

Detection of Camouflaged Targets in Cluttered Backgrounds using Fusion of Near Simultaneous Spectral and Polarimetric Imaging

August 9, 2000

**Rulon Mayer, Richard Priest, Christopher Stellman, Geoffrey Hazel,
Alan Schaum, Jonathon Schuler, and Michael Hess**

**Sensors and Data Analysis Section, Code 5621
Advanced Concepts Branch, Optical Sciences Division
Naval Research Laboratory
Washington, DC 20375**

Abstract

The detection of low signature or camouflaged targets in cluttered backgrounds is a crucial problem in tactical reconnaissance. In the past few years, imaging spectral and polarimetric sensors have been evaluated for this application. Although these sensors have separately generated promising results, each imaging modality alone appears to have not achieved the desired level of target detection. Fusion of data from multiple sensing modalities may potentially improve performance to acceptable levels. In the case of, a key issue is the correlation of the spatial location of the false detection within spectral and polarimetric imaging. This paper presents a study of a data set consisting of near simultaneous spectral and polarimetric images recorded from sensors collocated on North Oscura Peak in the White Sands test range. The sensors overlooked a scene composed of natural background, military vehicles, and camouflage material. The sensors operated in the visible band with nearly equal, simultaneous field of view. The RX anomaly detection algorithm was separately applied to each data set to obtain a two dimensional map of target and false detections. The paper will analyze the correlation of false detections for image fusion. Background segmentation of the hyperspectral and polarization data sets was also examined.

Introduction

Target detection amid natural background clutter can be achieved through collection and analysis of data derived from optical multispectral or hyperspectral sensors. The reflection or emission spectral signatures depend on the elemental composition of objects residing within the scene. Targets whose elemental composition deviates substantially from the backgrounds may be more easily detected using radiation wavelength selective detectors. Although the schemes applied to the optical spectral data are highly selective in discriminating targets, it is necessary to vastly improve the sensitivity. Detection of an additional feature of suspected targets has been postulated to help in discriminating objects within a given scene. Radiation polarization is sensitive to surface features such as relative smoothness or roughness¹. It has been suggested that detection of radiation polarization, in combination with radiation wavelength sensitivity maybe enhance target detection. The hyperspectral data were recorded to enable a preliminary assessment of the utility of polarimetric / hyperspectral data fusion. Mathematical fusion of data sets has been examined to enhance target detection using a different imager².

Report Documentation Page

Report Date 09082000	Report Type N/A	Dates Covered (from... to) -
Title and Subtitle Detection of Camouflaged Targets in Cluttered Backgrounds using Fusion of Near Simultaneous Spectral and Polarimetric Imaging	Contract Number	
	Grant Number	
	Program Element Number	
Author(s) Mayer, Rulon; Priest, Richard; Stellman, Christopher; Hazel, Geoffrey; Schaum, Alan; Schuler, Jonathon; Hess, Michael	Project Number	
	Task Number	
	Work Unit Number	
Performing Organization Name(s) and Address(es) Sensors and Data Analysis Section, Code 5621 Advanced Concepts Branch, Optical Sciences Division Naval Research Laboratory Washington, DC 20375	Performing Organization Report Number	
Sponsoring/Monitoring Agency Name(s) and Address(es) Director, CECOM RDEC Night Vision and Electronic Sensors Directorate, Security Team 10221 Burbeck Road Ft. Belvoir, VA 22060-5806	Sponsor/Monitor's Acronym(s)	
	Sponsor/Monitor's Report Number(s)	
Distribution/Availability Statement Approved for public release, distribution unlimited		
Supplementary Notes The original document contains color images.		
Abstract		
Subject Terms		
Report Classification unclassified	Classification of this page unclassified	
Classification of Abstract unclassified	Limitation of Abstract UNLIMITED	
Number of Pages 16		

A field collection of polarimetric image data was conducted during the period 12-16 October 1998 at North Oscura Peak, White Sands Missile Range, NM. The collection was coordinated by Nichols Research Corporation (NRC) and ERIM International. A Naval Research Laboratory (NRL) team recorded companion hyperspectral data using the Dark Horse 1 (DH1) sensor. A University of Alabama, Huntsville (UAH) visible spectrum polarimetric camera was operated by the NRC team.

This report concentrates on the data fusion analysis. Since the hyperspectral data was visible spectrum only, visible spectrum polarimetric data was the logical choice for fusion with the hyperspectral data. The UAH visible polarimetric camera was a good match in IFOV to the hyperspectral sensor. For this reason the UAH data set was chosen for detailed analysis.

In order to provide a context for the fusion analysis itself, an overview of the characteristics of the Dark Horse³ and UAH sensors is provided. The various steps in the data reduction chain are also outlined.

The final sections of the report summarize the results of the fusion assessment. It is found that data fusion based on "AND" processing provides the best results. Approximately one order of magnitude improvement in false alarm reduction appears to be possible from fusion of the two data sets.

Sensors

Several sensors were employed during the field test. NRC provided separate MWIR and LWIR imaging polarimeters, ERIM supplied a second MWIR imaging polarimeter and UAH provided a visible imaging polarimeter. NRL provided the DH1 visible hyperspectral sensor outfitted with a computer-controlled scanning table. Detailed descriptions of the polarimetric sensors are available in separate reports from NRC and ERIM. Some information on the DH1 sensor is provided here for easy reference. More detailed information is available from NRL. Since the polarimetric data of interest in this report was collected by the UAH instrument, a brief description of this instrument is contained below in the polarimetric analysis section. More information is available from UAH.

Hyperspectral Sensor (Dark HORSE)

The Dark HORSE hyperspectral imaging sensor³ consists of a standard 1" CCTV lens (Navitar, DO-5018), an $f/2$ imaging spectrograph (Instruments S.A., CP140) and a high-frame-rate CCD camera (Sarnoff, VCCD512). Imagery collected via the 50mm focal length lens is dispersed using a high throughput $f/2$ imaging spectrograph. The spectrograph employs an aberration-corrected concave holographic grating, providing a flat field spectral range from 400 to 850 nm. A 25 μm slit width was used for all data collections. However, it should be noted that the size of the binned CCD pixels (not the spectrograph slit width) defines the sensor's maximum spectral resolution of 7nm.

Digital collection of the hyperspectral imagery is achieved using a custom high-frame-rate CCD camera. The camera is a 16-port split frame transfer CCD with 12-bit digitizers operating at a maximum frame rate of 200 Hz. A custom high-frame-rate interface box is used to merge the 16 12-bit digital camera output channels into a single 32-bit channel that is then read via a digital frame grabber board (MuTech, MV-1100). The 512 x 512 silicon focal plane array (FPA) is capable of capturing digital hyperspectral data cubes with a maximum of 512 cross-track spatial pixels and 512 wavelength bands. During this field test the spectral pixels were binned via hardware to provide 64 wavelength bands. Spectral pixel binning provided adequate signal-to-noise levels at the relatively short integration times (0.1 seconds per frame) used for this collect. The instantaneous field of view (IFOV) is 0.22 mrad.

The sensor is controlled using a 266 MHz Pentium II PC and a custom software application run under the Microsoft Windows NT operating system. The user interface provides the user a means of entering required input parameters, such as archival file names, desired binning parameters and camera frame rates. In addition to controlling the sensor the controller computer is used to unscramble the frame grabber's 32-bit image output.

The sensor operates in a pushbroom mode by forming a spectrally dispersed image of the entrance slit onto the two-dimensional FPA. One dimension gives spectral information and the other dimension gives spatial information in the cross-track direction. Scanning the slit across the scene of interest gives spatial information in the down-track direction and results in a three-dimensional hyperspectral data cube. Typically, the required scanning motion is achieved by mounting the sensor to a moving airborne platform. For this data collection, motion in the down-track direction was achieved via a computer-controlled azimuth-elevation scanning mount. For all data collected the sensor was scanned at a rate of 0.125 degrees/sec while holding the elevation angle constant.

Sensor and Target Sites

All data were collected at North Oscura Peak, White Sands Missile Range, NM. All sensors were located at the top of North Oscura Peak at the "Atom Site". Sensors were placed on a concrete platform (previous page) that overlooked the "Target Site" (Figure 1). The "Target Site" was at the base of North Oscura Peak at a depression angle of approximately 30 degrees and a distance of approximately 1500 meters from the sensor platform.

Targets

A variety of targets were examined during the course of the field test, ranging from military vehicles to simple geometric shapes. For the purposes of

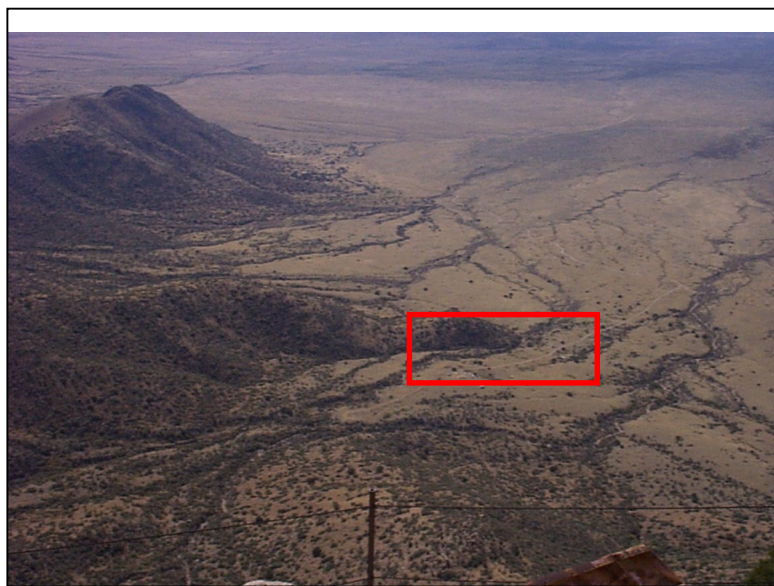


Figure 1. North Oscura target site.

this study, The Camouflage, Concealment and Deception (CC&D) related targets are the focus of this study. These targets included military vehicles, vehicle decoys, and Chemical Agent Resistant Coating (CARC) panels. The targets were positioned along a jeep trail and arranged such that the military vehicles were in pairs (Figure 2), with one vehicle obstructed (via natural or manmade cover) and one in clear view.



Figure 2. Enlarged picture of targets (indicated with lines).

General Observations

The DH1 sensor and system worked well over the course of the field test with no significant hardware problems. Poor field conditions (high winds, dust storms and lack of power) during the later portion of the week limited data collection to the first two days of the field test. Despite this limitation, a significant amount of data was collected. Most image scans covered the entire target region and a considerable amount of ground adjacent to the targets. Image scans were also collected both above and below the target region, with only a subset of the targets within the sensor's field of view.

In addition to the hyperspectral data, simultaneous video imagery was collected. Additionally, digital photos of all of the CC&D targets were acquired and a map of the targets' relative positions was drawn (see above). A detailed listing of the targets' exact geolocations with respect to the sensor is available through NRC and ERIM.

Wind was a constant concern during the course of the field test. Mild winds caused the scanning mount to sway during data collections, high winds made it necessary to abort data collections completely. During mild winds it was found that frame rates of 10 Hz provided the best results. At this rate, data were sampled rapidly enough to minimize image pixel smearing yet slow enough to avoid the use of high scan velocities. Scan rates higher than 10 Hz did not produce reliable data.

Spatial Correction

The spectrometer optical configuration which directs radiation to the focal planar array is not perfectly ideal. To correct spatial aberrations, the spectrometer is calibrated by exposing it to mercury and krypton lamps placed at fixed positions. Software corrects each pixel within the two dimensional array to generate a linear spatial response. This correction reduced the observed aberration from as much as 10 pixels in the outer regions of the focal plane array down to 1 pixel. Central portions of the array displayed much smaller spatial distortions.

Flat-fielding

Radiometric corrections to the raw data are also required because the spectrometer radiation transport efficiency depends on wavelength. Flat-fielding procedures were used to correct for the wavelength dependent responsivity. This software correction was applied to each pixel within the image following exposure to a spatially uniform radiation source of known intensity. The figures show profiles before and after flat-fielding corrections. After flat-fielding corrections were applied to the data editing limited the hyperspectral image set to data residing between the black vertical lines.

Destriping

The visible hyperspectral image contains “streak” artifacts (Figure 3a). Most of the streaks appear as lines that run along the in-track (horizontal) direction. These streaks are attributed to unstable electronics used to process signals in the CCD array. Additional instability is attributed to the variable, random movement of the Dark HORSE 1 spectrometer under windy conditions at the test site.

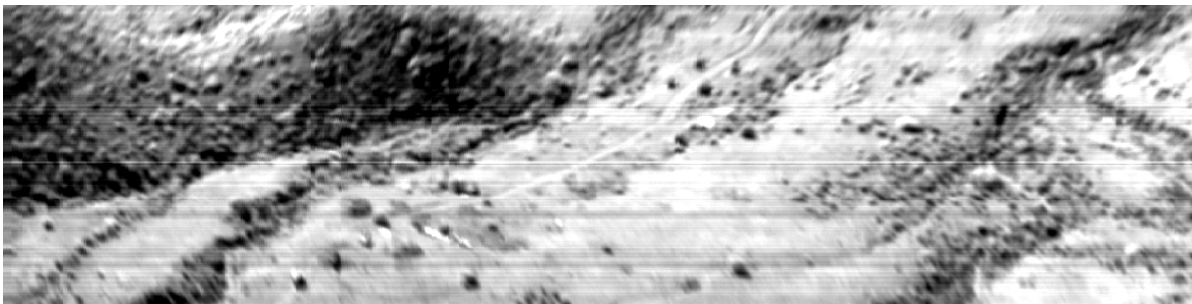


Figure 3a. Horizontal stripes displayed in one band within visible hyperspectral data cube.prior to “destriping”

The streaks are particularly deleterious for anomaly detection algorithms. The presence of regions showing sharp gradients will generate false anomalies. Figure 3b depicts the vertical profile (after taking the median in the horizontal direction) in bands 10, 20, 30.

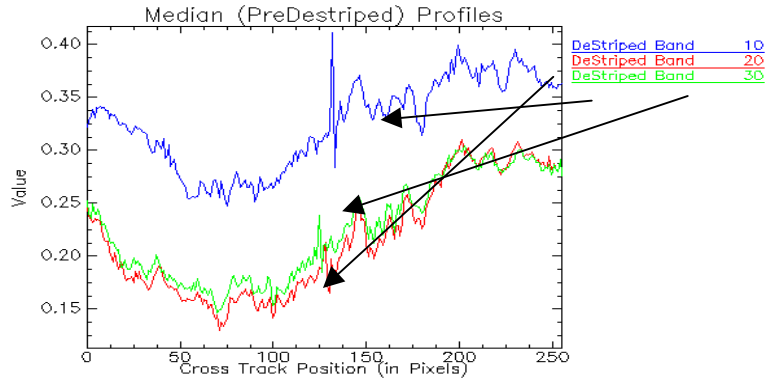


Figure 3b depicts the vertical profile (after taking the median in the horizontal direction) in bands 10, 20, 30.

To help enhance the search for anomalies, the streaking was ameliorated by post processing of the image set. Custom software reduced the apparent streaking by a complex procedure applied to each spectral band image. The method involved computation of the row medians, determination of the row offsets needed to produce the smoothed median profiles shown in the figure below, and finally correction of all the pixel values by these offsets. Following application of the destriping algorithm, the horizontal streaking was substantially reduced as seen in the image Figure 4a and the profiles shown in Figure 4b.

Figure 4a. Prominent horizontal stripes removed from band displayed in Figure 3a.

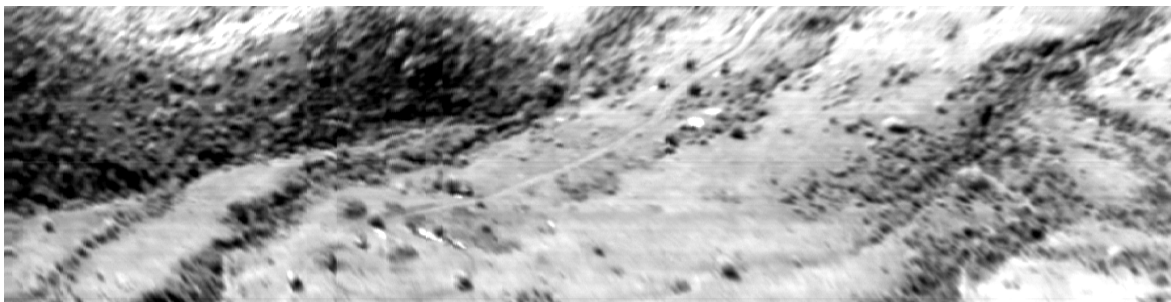
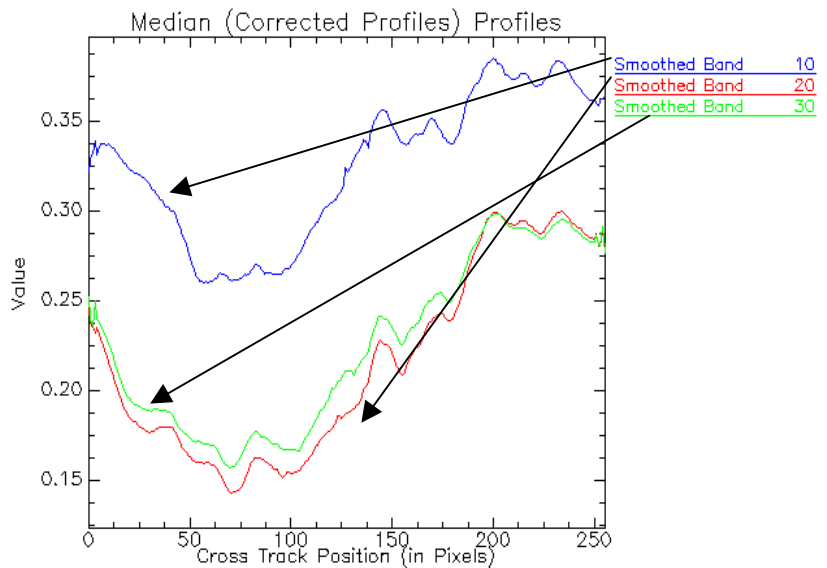


Figure 4b depicts the smoothed vertical profile (after taking the median in the horizontal direction) in bands 10, 20, 30.



Additional Editing of the Hyperspectral Data

Following flat fielding and spatial distortion corrections, the hyperspectral image data set required further editing. Although the calibrations corrected most distortions, image editing was still required to provide a valid image set. Specifically, the image set was reduced from 512 pixels in the cross track direction down to the central 256 pixels. Additionally, spectral bands 1-6 and 50-64 were eliminated due to remaining distortions. The remaining bands (7-49), correspond to the spectral range 820-500 nm.

Polarimetric Analysis

Stokes images can be used to characterize the degree of linear and circular polarization at each individual pixel within a digital image scene^{4,5}. The individual Stokes parameters are S_0 (total intensity), S_1 and S_2 (linear polarization), and S_3 (circular polarization). The University of Alabama, Huntsville polarimetric camera was used to collect the polarimetric data. The key elements of this camera are a 320 x 192 element CCD array positioned behind a rotating retarder plate / fixed polarizer combination. The IFOV is .23 x .26 mrad. In the field, the retarder was rotated to 12 angular positions separated by intervals of 15 degrees and an image, $I(n)$, was recorded for each position. The 12 images were spatially registered to each other using custom software based on tiepoints and polynomial fitting. The 12 images are related to the Stokes images and degree of linear polarization (DOLP) in the following manner.

$$I(n) = \frac{S_0}{2} \left[1 + \frac{DOLP}{2} \cos(2\theta - 2\psi) \right] + \frac{S_3}{2} \sin(2\theta - 2\psi + \frac{\pi}{12} 2n) + \frac{S_0 DOLP}{2} \cos(4\theta - 2\varphi - 2\psi - \frac{\pi}{12} 4n)$$

$$n = 0, 1, 2, \dots, 11$$

θ = orientation of fast axis when $n = 0$; same for all pix

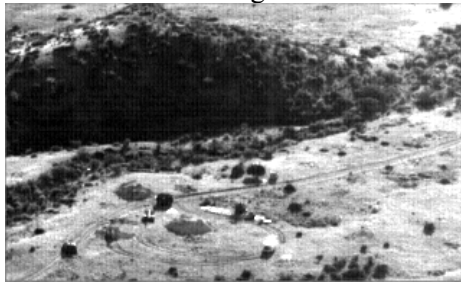
$\psi = 0$ = orientation of analyzer, same for all pix

φ = orientation of linear comp. of pol.

$$DOLP = \sqrt{S_1^2 + S_2^2} / S_0$$

The Stokes images were computed by inverting this equation. Imperfect registration generated some artifacts in the Stokes images (especially S_3). Improvements in registration would be desirable. Shown below (Figure 5) are processed Stokes images derived from the UAH polarimeter. The S_1 and S_2 images (Figure 5b, 5c) suppress clutter significantly while permitting observation of some of the targets in the scene. A number of targets were not detected.

S_0



S_1

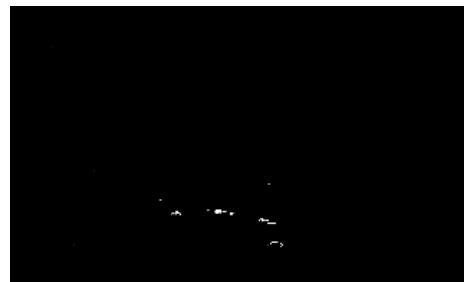


Figure 5a. S_0 Stokes image

Figure 5b. S_1 Stokes image

S_2



Figure 5c. S_2 Stokes image

S_3



Figure 5d. S_3 Stokes image

Registration of Hyperspectral Images with Polarimetric Images

The hyperspectral images are generally similar to the polarimetric images. However, the overlap between the two sets of images is not perfect and consequently some manipulation of the image set was required. We adopted the strategy of warping the hyperspectral images to the polarimetric images. This involved translation, rotation, magnification, and resampling of the hyperspectral images to achieve a 1 to 1 correspondence between hyperspectral pixels and polarimetric pixels. Part of this process is spatial co-registration of the two sets of images. To register the data, common points called ground control points (GCP) were identified within each image set. These reference points were used to connect the two sets together. A total of 7 ground control points were employed. Since our linear registration method required four GCPs, three remained to assess the quality of the registration. Typically, the hyperspectral and polarimetric image sets were registered to within <0.8 pixels. The final result of the warping process was an 320×192 pixel image size for both data sets.

RX anomaly detection

Manmade targets located within natural backgrounds often appear as spectrally anomalous objects. However, the detailed spectral signature of the target is usually not available a priori. Anomaly detection algorithms, such as the RX algorithm⁶, search for pixels within the image set exhibiting a spectrum significantly different from that of the background. The RX value for the pixel at a row, column position i,j is

$$RX(x_{ij}) = (x_{ij} - \text{mean})^T * (M^{-1}) * (x_{ij} - \text{mean})$$

where x_{ij} is the spectral vector at position i,j , mean refers to the mean band value, and M^{-1} is the inverse of the covariance matrix. Figure 6 pictorially outlines the RX anomaly search process.

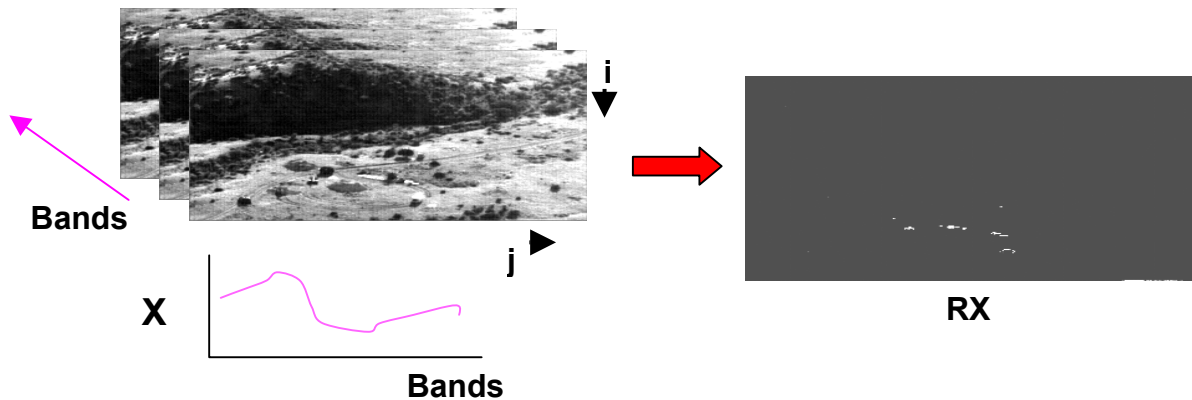


Figure 6 pictorially outlines the RX anomaly search process.

The “three-dimensional” image cube (having 40 bands in the hyperspectral image set) is thus reduced to a two dimensional RX map displaying the degree of anomaly within the image. Relatively large RX values are to be associated with detections (either true or false). Images useful for diagnostics can be created by thresholding the RX maps to show the pattern of detections. A further refinement is to overlay an image mask corresponding to the known position of the real targets. Maps created in this way from the hyperspectral data and for the polarimetric data are shown in Figures 7a, 7b. The known target overlays are in color. The white areas are false detections. Raising the threshold decreases the number of false detections at the expense of missing more true targets. In generating these images a preprocessing step called principal component analysis was used. This statistical tool is discussed in more detail below. Principal components (PC) 2 through 7 were used for the hyperspectral data and PCs 2 and 3 were used for the polarimetric data.

Figure 7a Target mask superimposed on RX output from HSI data.

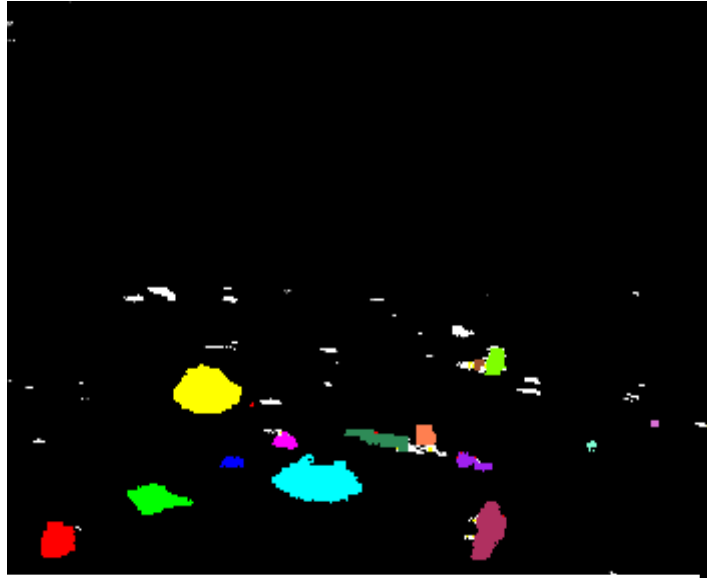
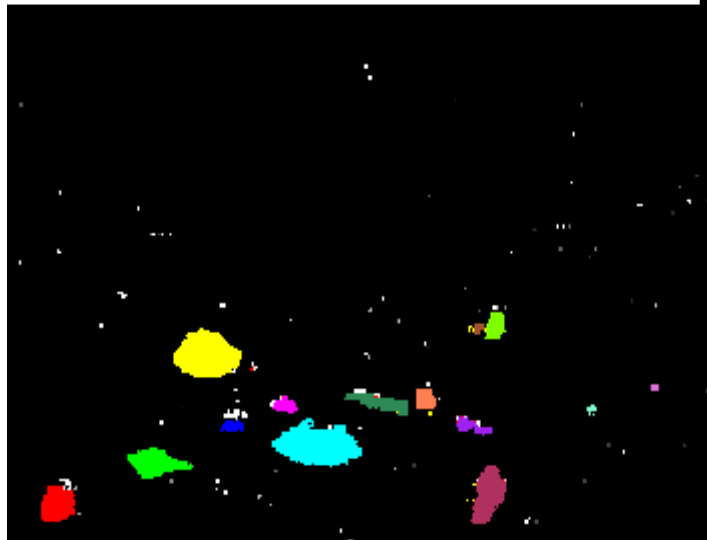


Figure 7b Target mask superimposed on RX output from polarization data.



ROC Curve

Receiver Operating Characteristic (ROC) curves are used to visualize a classifier's performance and to aid in selecting the proper decision threshold. To generate a ROC curve, a series of detection results for different threshold values are compared with ground truth information in order to determine how many detections are true and how many false. Each pixel within the image is examined to determine whether or not the RX output value at that pixel exceeds a given threshold and, if so, whether the pixel resides within the ground truth region of interest (ROI) corresponding to one of the targets. The ROC curves display the target detection probability versus probability of false detection. Individual target ROIs typically contain multiple pixels. In

this study, a target was considered to have been detected if any pixel within a target ROI exceeded a given threshold value. The percentage of false detections is defined as the percentage of pixels lying outside all target ROIs with RX value exceeding the threshold value.

Principal Component analysis

The hyperspectral data set has 40 bands of spectral information. From a statistical point of view, this corresponds to 40 degrees of freedom. Past experience has shown that the effective number of independent degrees of freedom is far less – typically on the order of 6 or 7. Principal component (PC) analysis is a convenient way to reduce the data set to a dimension of this order and separate image information from noise. The method works by forming orthogonal linear combinations of the 40 band images and ranking these combination images by variance. PC 1 (highest variance) is usually close to the arithmetic average of the 40 bands. Since it is nearly an average, it is dominated by background clutter and is usually discarded. The PCs with the lowest variance (e.g 37th, 38th, 39th and 40th) are dominated by noise and so are not useful. Best results in this study were obtained by retaining PC 2 through 7. This choice has several advantages. It rejects a good deal of “ordinary” clutter (contained in PC 1). It reduces remaining streaks and rejects some of the sensor noise (contained in PCs 8-40). It reduces the size of the data set thereby easing computational requirements. The PC algorithm itself is not computationally intense.

The same idea can be applied to the polarimetric data set. The initial data set is 4 dimensional in this case (S_0, S_1, S_2, S_3). The S_0 component was rejected because it is clutter dominated. PC analysis was applied to the remaining 3 components. The last PC is nearly equal to S_3 (mostly noise and artifacts). It was rejected and the other two PC were retained.

Fusion of Hyperspectral Images with Polarimetric Data .

Two sets of independent imaging modalities, visible hyperspectral and polarimetry, viewed a common set of targets and backgrounds. These two image sets depict common targets but differing false alarms. Combining imaging modalities, or fusing the data, was investigated as a possible way to enhance target detection for constant false alarm rates. There are a variety of ways to fuse registered sets of images. Four possibilities are examined below. It was not possible to use data recorded at the same time from the two sensors for this exercise. There was no time when the UAH polarimetric camera and the DH1 spectral sensor were both functioning well. Fortunately the scene did not change very much during the course of the test. The hyperspectral scene used was recorded on Oct 13 at 1 pm. The polarimetric scene used was recorded on Oct 12 at 5:40 pm.

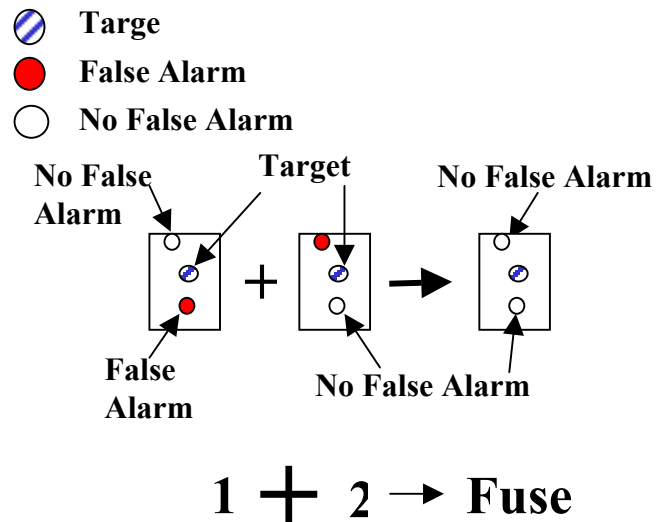


Figure 8a. Schematic showing fusion algorithm using summation of RX output from HSI and polarization.

Sum RX Images

In this approach, the RX anomaly algorithm was run separately on the hyperspectral and polarimetric data. In the case of the polarimetric set, only S_1 , S_2 , and S_3 were used in the data set because S_0 (total intensity) was clearly dominated by clutter. An “OR” type of fusion can be implemented simply by summing the RX outputs (Figure 8a). This is referred to as “OR” processing because anomalies in either data set have a good chance of being selected as detections.

shown Figure 8b is the effective ROC curve from summing the individual RX outputs of the hyperspectral, and polarimetric imaging sets. Summing the RX outputs (at the pixel level) of the hyperspectral (HSI) and polarization data results in a modest enhancement in the detection of targets at constant false alarm rate.

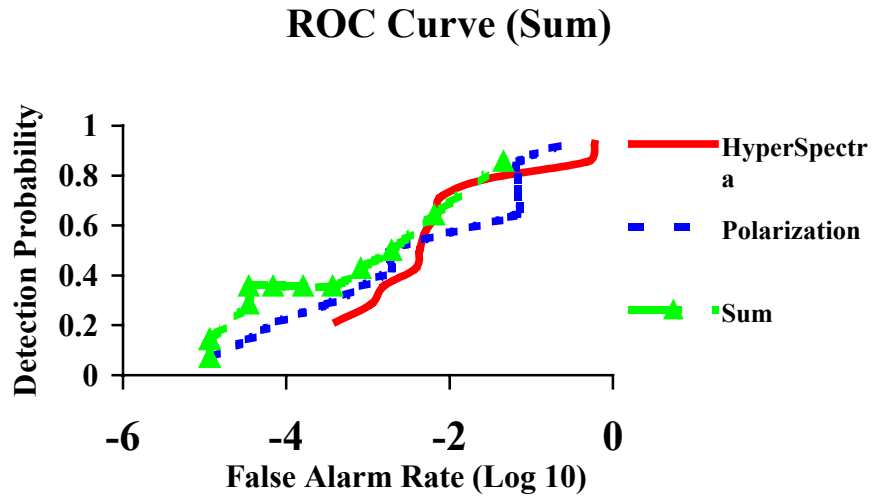


Figure 8b. ROC curves showing fusion, HSI, and polarization

The hyperspectral set was taken from 40 bands (following editing) and selecting the principal components (PC) 2 through 7 (in order of decreasing eigenvalue and variance). The polarimetric set was derived using Stokes images S_1 , S_2 , S_3 (S_0 was excluded as being clutter-dominated).

1. Multiply RX Images

Observation of many uncorrelated false detections in the RX output from the hyperspectral and polarimetric image sets suggests another way of fusing the data to enhance target detection. Instead of summing the data, the two RX images can be multiplied at the pixel level with the idea of suppressing false detections not present in both RX images. This approach is sometimes denoted as the “AND” algorithm because only pixels anomalous in both data sets are likely to be selected as detections.

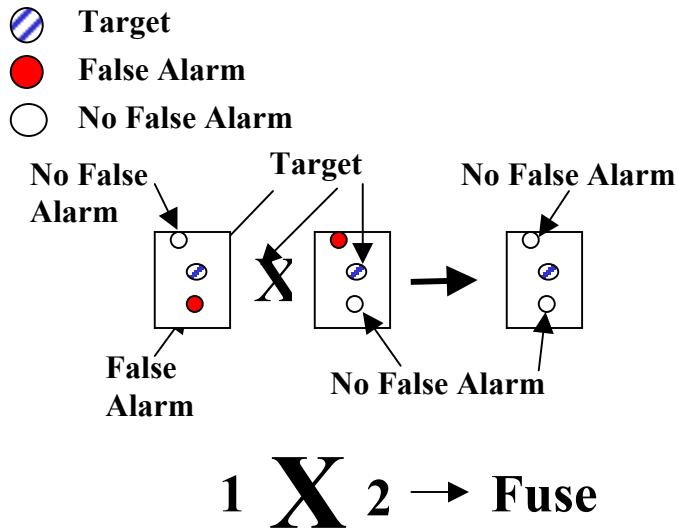


Figure 9a. Schematic showing multiplication of HSI and polarization to fuse data.

Figure 9b is the effective ROC curve derived by multiplying the individual RX outputs of the hyperspectral (HSI), and polarimetric imaging sets. Multiplying the outputs (at the pixel level) of the hyperspectral and polarization data results in greater enhancement in the detection of targets at constant false alarm rates than does summing the image sets.

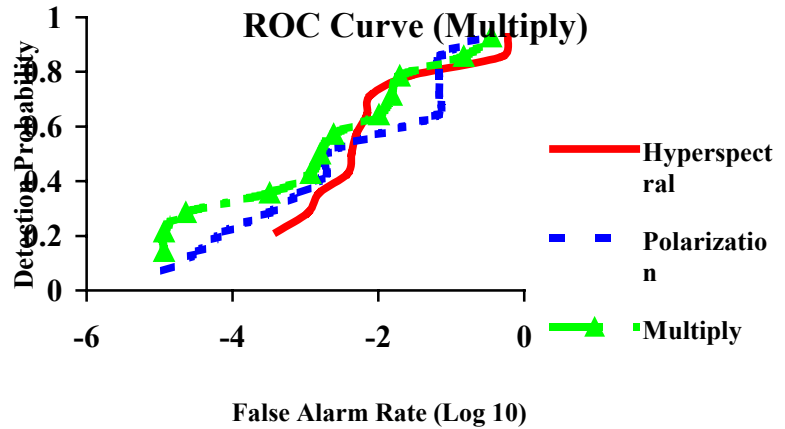


Figure 9b ROC curve from multiplication fusion, HSI, and polarization

3 Combine Hyperspectral and Polarimetric data sets and perform Anomaly Detection on large image set

A third approach (illustrated by Figure 10a) tried to combine the hyperspectral image set with the polarimetric image set to form a 42 dimensional data set (only S_1 and S_2 images were used). The PC transformation was then performed, and only PC 2 – 7 retained. The RX algorithm was then run on this 6 dimensional data set. This approach is motivated by the idea that the large data set might be characterized by joint Gaussian statistics.

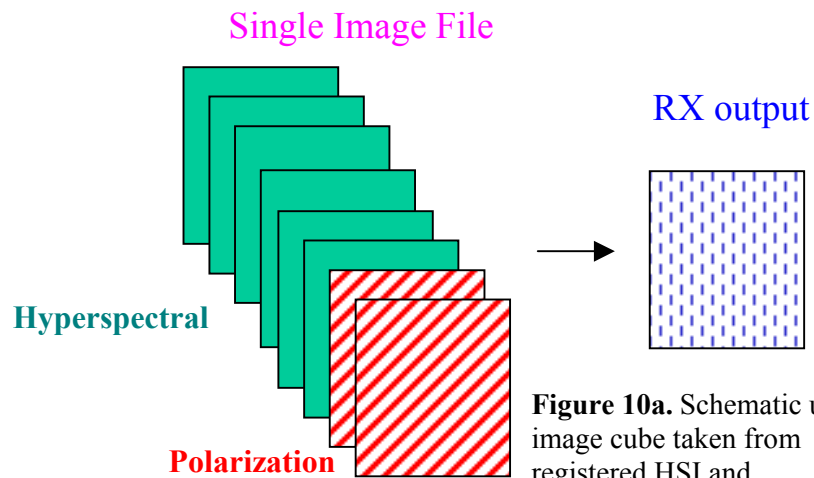


Figure 10a. Schematic using image cube taken from registered HSI and polarization data sets.

Figure 10b shows the effective ROC curve from performing an RX calculation on a combined image set. The large image set is generated by combining 40 bands from the hyperspectral set with the S_1 and S_2 images from the polarization set. The RX algorithm was subsequently applied using principal components 2 through 7 (in

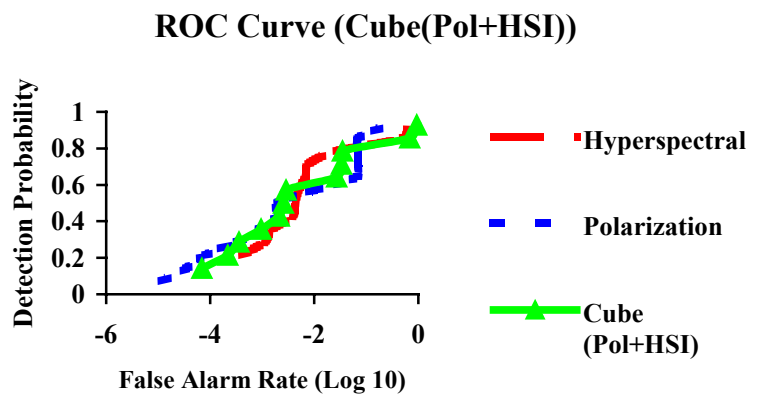


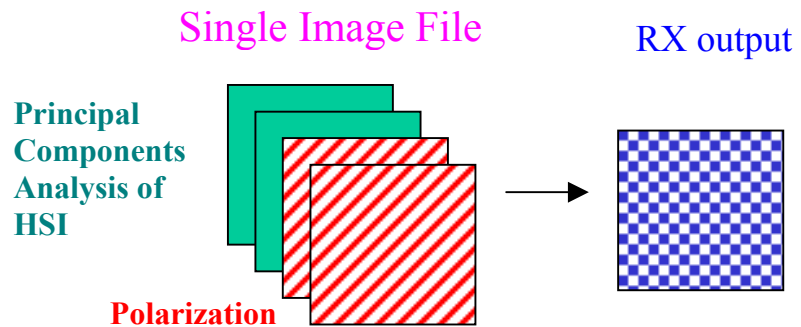
Figure 10b. ROC curve from registered cube, HSI, and polarization

order of decreasing eigenvalue and variance). As a comparison, the hyperspectral (HSI), and polarimetric RX outputs are also shown. Performing the RX on the combined image set results in no significant improvement in the detection of targets at constant false alarm rates.

4. Combine Principal Component Analysis of Hyperspectral data with Polarimetric data and perform Anomaly Detection on large Image Set

The fourth approach tried was a variant of the third. The PC transformation was applied to the hyperspectral (HSI) data set before combining the data sets (Figure 11a). The motivation here is to optimize the hyperspectral data set before fusion. Figure 11b shows the effective ROC curve obtained in this way. The large image set is generated by combining PCs 2 through 7 from the hyperspectral set and Stokes images S_1 and S_2 from the polarimetric set. The RX algorithm was applied using (PC) 2 through 7 (in order of decreasing eigenvalue and variance). As a comparison, the hyperspectral (HSI), polarimetric RX outputs are also shown. Performing the RX on the combined image set results in no significant improvement in the detection of targets at constant false alarm rates.

Figure 11a. Schematic showing fusion involving PC from HSI forming a cube with polarization



ROC Curve (Cube(Pol+PC HSI))

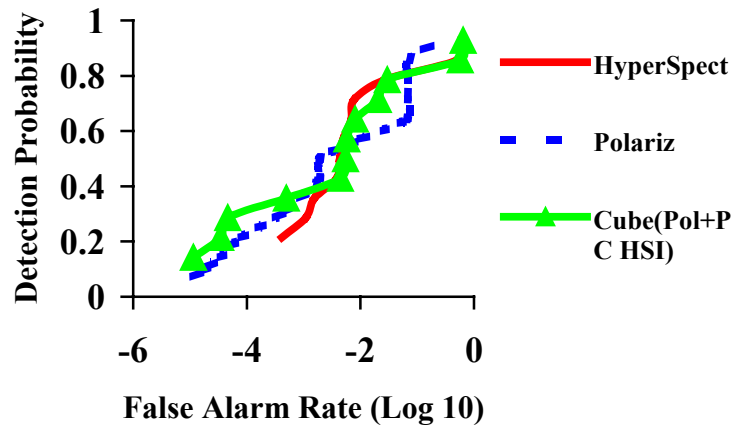


Figure 11b. ROC curve showing fusion from PC reduced HSI and nolarization HSI and nolarization

RX Scatter Plot

Additional insight may be achieved by generating a scatterplot of the registered RX outputs from the hyperspectral imager and polarimetric camera. The graph plots the pixel value of the registered RX output from the hyperspectral image set against the pixel value of the RX output from the polarimetric data. It can be shown (figure not shown) that low RX values from the polarimetric data correlate with higher RX values from the hyperspectral imager. Conversely, pixels with high RX values from the polarization data correspond with low RX values from the hyperspectral imager. In addition, it can be noted that pixels showing high polarization anomaly and low hyperspectral anomaly values tend to appear at the edges of targets while those with low polarization anomaly and high hyperspectral anomaly values tend to appear in the central area.

Used in this way, hyperspectral and polarized images may complement each other in detecting targets in the clutter.

Preliminary Fusion of Clustered Image Cubes

This paper has examined searches for anomalies within the background clutter. Clustering of the background clutter provides another approach for analyzing the data. A preliminary examination of clustering the clutter is summarized.

Prior to segmentation of the hyperspectral visible data, illumination suppression⁷ was applied to all pixels within the image cube. Figure 12 illustrates illumination suppression in two dimensions. The first principal component direction depicts the region of highest variance and presumably runs parallel to the illumination direction. Surfaces orthogonal to first principal component therefore depict regions of constant illumination. The surface of constant illumination was chosen to intersect the mean value. Each pixel was projected onto a hypersurface using the virtual shade point (minimum pixel value). Prior to shade correction, a median filter was applied to the hyperspectral image cube to eliminate singularities generated in the projection.

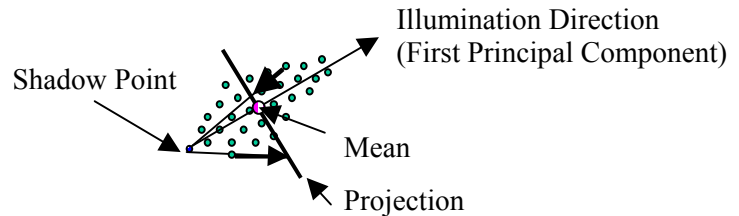
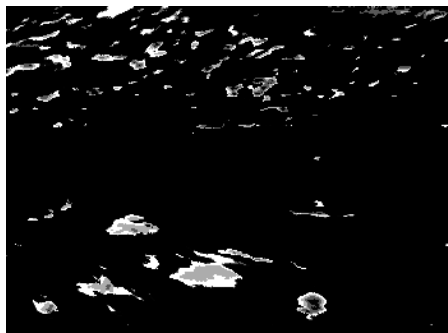


Figure 12. Illumination equalization method illustrated.

Background clutter clustering is achieved by using the unsupervised classifier k-means⁸. The hyperspectral visible spectra was partitioned into six clusters plus a cluster composed of pixels residing beyond the fixed distance from the designated cluster means. The partitioned regions correspond to targets (Figure 13a). Similarly, the S1 and S2 components from the registered visible polarimetric data were partitioned into two components plus the null segment (null segment shown in Figure 13b).

HSI, 6 Clusters



Polarization, 2 Clusters



Figure 13. Segmented output from HSI (a) and polarization (b)

Fusion was accomplished by multiplying the two sets of registered segmented data sets on a pixel by pixel basis (see Figure 9b). To evaluate the potential gain from this version of data fusion, ROC curves were generated from the previously used target masks. Again, the false alarms in the data sets were uncorrelated and some enhancement (reduction of

FAR by one order of magnitude at 60% target detection level) in the data can be achieved using these independent data sets. Other clustering schemes, such as those testing supervised classification algorithms and number of segments are being investigated.

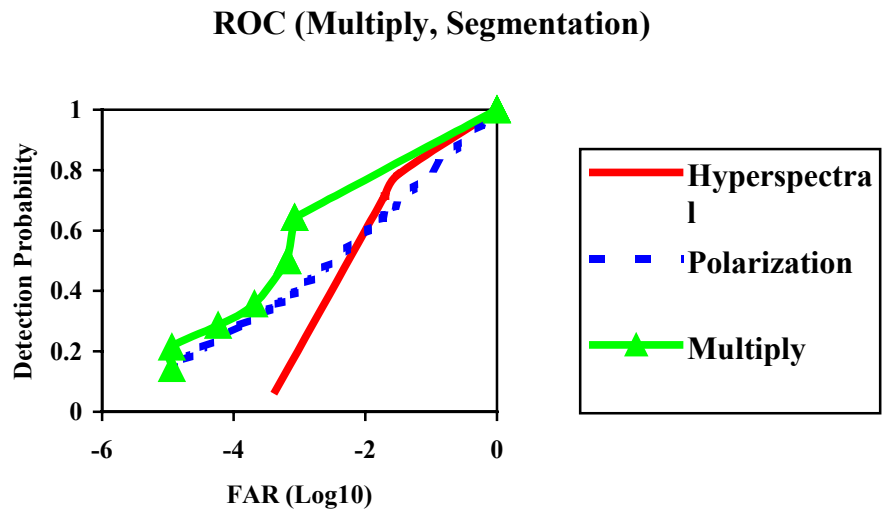


Figure 14. ROC curve comparing multiplied segmented HSI and polarization and segmented HSI, and polarization.

Summary and Conclusion

Using ground control points to register the hyperspectral and polarimetric image data, the data sets were combined in a variety of ways. The best ROC curve results were obtained with the “AND” algorithm. Thus, it appears that false alarms are largely uncorrelated in the two types of imaging modalities. A more modest ROC curve benefit was obtained with the “OR” algorithm. Combining image cubes does not appear to enhance the detection of targets at constant false alarm rates. Scatter plots reveal that polarimetric RX anomaly imagery tends to detect the edges of targets while the hyperspectral methods preferentially select the central regions. This suggests that the two modalities may complement each other, particularly in target segmentation or image understanding.

Confidence in these results is limited by the quality of the hyperspectral image and polarization data sets. Destriping reduced or eliminated spurious streaks in the hyperspectral images, but there remained a number of artifacts in the data that appeared as false detections. These artifacts also precluded the use of matched filter hyperspectral detection algorithms since these methods are particularly susceptible to artifacts, especially in combination with illumination equalization. This study would have benefited from availability of better quality hyperspectral data. Benefit also would have been gained from better internal registration of the raw polarimetric image set. Suboptimal registration led to some artifacts in the polarimetric data set.

Reference :

1. T. Rogne, S. Stewart, and M. Metzler “Infrared Polarimetry: What, Why, How, and the Way Ahead” Proc. NATO-IRIS Vol **43**, No. 2, p 357-368 (1998).
2. W. Barker, S. Mori, E. Sullinger, M. Boe, “Data Fusion of the Multi-spectral Sensor Surveillance System (M4S)” Proc. NATO-IRIS Vol **43**, No. 1, p 25-42 (1998).
3. C. Stelman, F. Bucholtz, J. Michalowicz, “Dark HORSE 2 Quick-Look Report: Real-time detection of military ground targets using an infrared hyperspectral imaging sensor” NRL Technical Report, NRL/MR/5621-99-8364, April 1999.

4. D. Clarke and J.F. Grainger, Polarized Light and Optical Measurements, Pergamon Press, Oxford (1971)
5. J.L. Pezzaniti and R.A. Chipman, "Imaging Polarimetry for Optical Metrology", Proceeding of SPIE, vol 1317 , p. 280-294 (1990)
6. I. Reed, X. Yu, "Adaptive multiple-band CFAR detection of an optical pattern with unknown spectral distribution" IEEE Trans. on Acoustics, Speech, and Sig. Proc. **38**, 1760-1770 (1990).
7. E. Ashton, G. Hazel "Feature Extraction and multispectral classification in multispectral imagery", Proc. IRIS, CCD 1998 Vol 44000-117-X(1) 353-366 (1999).
8. J.A.Richards, "Remote Sensing Digital Image Analysis", Springer-Verlag, Berlin, (1994).